Turning graphene into an intensity gauge for Angle-Resolved Photoemission Spectroscopy

Cedric Schmitt,[1,2] Hans Kirschner,[3] Jonas Erhardt,[1,2] Lukas Gehrig,[1,2] Philipp Keßler,[1,2] Kilian Strauß,[1,2] Merit Spring,[1,2] Bing Liu,[1,2] Stefan Enzner,[2,4] Alexander Gottwald,[3] Vitaliy Feyer,[5,6] Timur Kim,[7] Cephise Cacho,[7] Chris Jozwiak,[8] Aaron Bostwick,[8] Eli Rotenberg,[8] Lukasz Plucinski,[5,9] F. Stefan Tautz,[10,11,12] Ralph Claessen,[1,2] Serguei Soubatch,[10,11] and Simon Moser[1,2,13,14,*]

[1]*Physikalisches Institut, Universität Würzburg, 97074 Würzburg, Germany*
[2]*Würzburg-Dresden Cluster of Excellence ctd.qmat, Universität Würzburg, 97074 Würzburg, Germany*
[3]*Physikalisch-Technische Bundesanstalt (PTB), 10587 Berlin, Germany*
[4]*Institut für Theoretische Physik und Astrophysik, Universität Würzburg, 97074 Würzburg, Germany*
[5]*Peter Grünberg Institut (PGI-6), Forschungszentrum Jülich, 52425 Jülich, Germany*
[6]*Faculty of Physics and Center for Nanointegration Duisburg-Essen (CENIDE), Universität Duisburg-Essen, 47047 Duisburg, Germany*
[7]*Diamond Light Source, Harwell Science and Innovation Campus, Didcot OX11 0DE, United Kingdom*
[8]*Advanced Light Source, Lawrence Berkeley National Laboratory, Berkeley, California 94720, USA*
[9]*Institut für Experimentalphysik II B, RWTH Aachen University, 52074 Aachen, Germany*
[10]*Peter Grünberg Institut (PGI-3), Forschungszentrum Jülich, 52425 Jülich, Germany*
[11]*Jülich Aachen Research Alliance (JARA), Fundamentals of Future Information Technology, 52425 Jülich, Germany*
[12]*Institut für Experimentalphysik IV A, RWTH Aachen University, 52074 Aachen, Germany*
[13]*Experimentalphysik IV—AG Oberflächen, Ruhr-Universität Bochum, 44801 Bochum, Germany*
[14]*Thin Films & Physics of Quantum Materials, Faculty of Physics, Bielefeld University, 33615 Bielefeld, Germany*

(Received 23 March 2026; accepted 5 September 2026; published 22 October 2026)

Angle-resolved photoemission spectroscopy (ARPES) provides the most direct experimental access to electronic band structures and many-body interactions in solids. Beyond energy and momentum, the measured intensity also carries detailed information about the initial-state wavefunction through the complex photoemission matrix element governing the transition to—and scattering character of—the photoelectron final state. Orbital tomography seeks to exploit this sensitivity to reconstruct electronic wavefunctions. However, its quantitative implementation has been hindered by the lack of direct information on the phase of the matrix element and by the nontrivial role of solid-state scattering. Here, we overcome these limitations by achieving an experimental reconstruction of the complex photoemission matrix element in quasi-freestanding monolayer graphene (QFMLG), including both amplitude and phase. By combining circular-dichroism ARPES with linearly polarized measurements within a controlled scattered-wave framework, we determine the full matrix element over a broad kinetic-energy range. The reconstructed amplitudes exhibit pronounced channel-selective resonances and Cooper minima, directly revealing substantial solid-state modifications beyond commonly used simplified models. Leveraging this quantitative reconstruction, we establish QFMLG as an easily available *in situ* intensity reference for ARPES. Its known complex matrix element enables direct normalization for the product of photon flux and detector response, allowing the determination of photoemission cross sections in other materials under identical experimental geometries. This advances orbital tomography by ARPES to a quantitatively normalized approach that separates the initial-state wavefunction from final-state scattering contributions, and more broadly may provide access to the associated quantum geometry.

DOI: 10.1103/7ddz-xy1y

I. INTRODUCTION

The prospect of using angular distributions of photoemitted electrons to reconstruct both the amplitude and the phase of electronic wavefunctions—and, more broadly, to access their quantum-geometric properties in Hilbert space—has recently attracted substantial interest [1–7]. Yet, the measured photoemission intensity per solid angle $\Delta\Omega$,

$$\frac{I(k_f, \Omega_{\boldsymbol{k}_f}; h\nu, \boldsymbol{\epsilon})}{\Delta\Omega} \propto \chi(k_f)\, I_{\mathrm{ph}}(h\nu, \boldsymbol{\epsilon})\, \frac{d\sigma}{d\Omega}(k_f, \Omega_{\boldsymbol{k}_f}; h\nu, \boldsymbol{\epsilon}), \quad (1)$$

is determined not only by the intrinsic electronic structure, but also by instrumental and geometrical factors. Specifically, it depends on the detector efficiency $\chi(k_f)$, the photon flux $I_{\mathrm{ph}}(h\nu, \boldsymbol{\epsilon})$, and the differential photoemission cross section $\frac{d\sigma}{d\Omega}(k_f, \Omega_{\boldsymbol{k}_f}; h\nu, \boldsymbol{\epsilon})$.

*Contact author: simon.moser@uni-bielefeld.de

Published by the American Physical Society under the terms of the Creative Commons Attribution 4.0 International license. Further distribution of this work must maintain attribution to the author(s) and the published article's title, journal citation, and DOI.

The differential cross section, in turn, is proportional to the modulus squared of the dipole transition matrix element $M_{\boldsymbol{k}_f\boldsymbol{k}}$. It is thus dependent on a given experimental configuration defined by the photon energy $h\nu$, light polarization $\boldsymbol{\epsilon}$, and the photoelectron wave vector $\boldsymbol{k}_f = (k_f, \Omega_{\boldsymbol{k}_f}) = (k_f, \theta, \phi)$, i.e., by the outgoing photoelectron's kinetic energy $E_{\text{kin}} = \hbar^2 k_f^2/2m$, polar angle θ, and azimuth ϕ. Consequently, the measured intensity reflects not only the symmetry and orbital character of the initial state $\psi_{\boldsymbol{k}}$, but also the nature of the photoelectron final state $\psi_{\boldsymbol{k}_f}$ and its scattering within the solid.

In the high-kinetic-energy limit, where the interaction of the photoelectron with the ionic core can be neglected, the final state is often approximated by a plane wave [8,9]. Under this approximation, the dipole matrix element simplifies to the Fourier transform of the initial-state wavefunction [1,3]. This leads to a conceptual framework in which the photoemission cross section parallels the structure and form factors familiar from neutron and x-ray scattering, reflecting the spatial arrangement and orbital shape of the initial states [1]. While this perspective dates back several decades [10–14], it has recently regained attention as a foundation for using angle-resolved photoemission spectroscopy (ARPES) as a tool to reconstruct molecular orbitals of planar organic molecules [2,7,15], to measure the electron density in the real space [16,17], and to probe more complex quantum properties of crystalline systems—such as orbital angular momentum (OAM) [4], Berry curvature [5], and even the full quantum-geometric tensor [6].

However, this idealized plane-wave approximation (PWA) is well known to be incomplete. Theoretical and experimental studies have demonstrated that the PWA fails to account for key phenomena, including circular dichroism (CD) in ARPES (CD-ARPES) [18], and cannot capture the rich interference and scattering effects between photoemission channels [19,20]—even in minimal two-dimensional (2D) systems such as the Dirac semimetal graphene [21] or the quantum spin Hall insulator indenene [22]. Nevertheless, these limitations can be overcome, at least to some extent. A modest yet powerful extension of the PWA—the scattered-wave approximation (SWA) that incorporates kinetic-energy-dependent amplitude and phase variations for the individual dipole-allowed photoemission channels—proves sufficient to reconcile many of these discrepancies [18,21].

In previous work, we have shown that, in the case of QFMLG's C $2p_z$ orbitals, the photoemission amplitude of the s and d channels can be reconstructed directly from experimental ARPES data obtained using only linearly polarized light, provided a photon-flux-calibrated source is used [21]. However, the relative phase between these channels remained experimentally inaccessible.

Here, we overcome this limitation by incorporating CD-ARPES measurements, which allow us to access the missing phase information [4,18]. This enables the full reconstruction of the s and d channels' photoemission components in QFMLG, forming what can be considered a model representation of photoemission from its π bands. Armed with this detailed understanding, we demonstrate that QFMLG can function as an *in situ* intensity reference for ARPES—a standard that permits correction of measured band intensities for photon flux and detector efficiency under arbitrary experimental geometries and at typical photoemission endstations.

To demonstrate the practical utility of this framework, we apply it to a monolayer of indium on SiC, the quantum spin Hall insulator (QSHI) indenene. Using QFMLG as an *in situ* intensity reference, we correct the kinetic-energy-dependent photoemission signal of indenene for detector efficiency and photon flux, thereby directly extracting the differential cross section of its valence band up to a constant factor.

Importantly, the intrinsic energy selectivity of the photoelectron final state acts as a spectral filter, suppressing contributions from higher-order or parasitic radiation ("false light") in the photon flux. This overcomes a limitation inherent to conventional flux-monitoring schemes based on semiconductor photodiodes or mirror currents [7], and enables reliable, energy-resolved cross section determination under standard synchrotron conditions.

Owing to the widespread availability of large-area epitaxial QFMLG, together with its environmental stability and long-term durability [23,24], QFMLG is uniquely suited to serve as a robust and transferable standard for quantitative ARPES intensity normalization. Positioned directly at the sample location and in exactly the same experimental geometry (light incidence and polarization as well as detector position) as the target system, it provides a direct reference for quantitative intensity normalization.

Because accurate, energy-resolved intensity calibration—such as realized at the insertion-device beamline of the Metrology Light Source (MLS) at Physikalisch-Technische Bundesanstalt (PTB) Berlin [25]—is experimentally demanding and not available at most synchrotron facilities, this strategy removes a central obstacle to determining differential photoemission cross sections. In perspective, it enables quantitative access to both amplitude and phase of the complex matrix element, and thereby to the associated quantum-geometric properties of electronic bands.

II. EXPERIMENTAL METHODS

A. Sample preparation

In-QFMLG (graphene/In/SiC) samples were grown following the recipe in Ref. [26]. Nitrogen-doped 4H-SiC substrates were dry etched in hydrogen, resulting in an atomically flat, oxygen-free (1 × 1) SiC(0001) surface [27,28]. Subsequently, the characteristic $(6\sqrt{3} \times 6\sqrt{3})$R30° reconstruction of zero-layer graphene (ZLG) was achieved by heating the SiC substrate in 950 mbar Ar atmosphere to 1365 °C for 10 min. Indium was intercalated by evaporating high-purity indium (⩾99.9999%) from a Knudsen cell maintained at 775 °C. The indium atoms lift the ZLG from the substrate, forming quasi-freestanding graphene [26,29]. The intercalation process itself involves two steps [30]. Initially, indium atoms were evaporated for 10 min at room temperature, followed by postannealing at 500 °C for 20 min. This cycle was repeated 5 times and concluded with a flash annealing at 800 °C for 10 s. The stability of these intercalated In-QFMLG samples permitted to transport

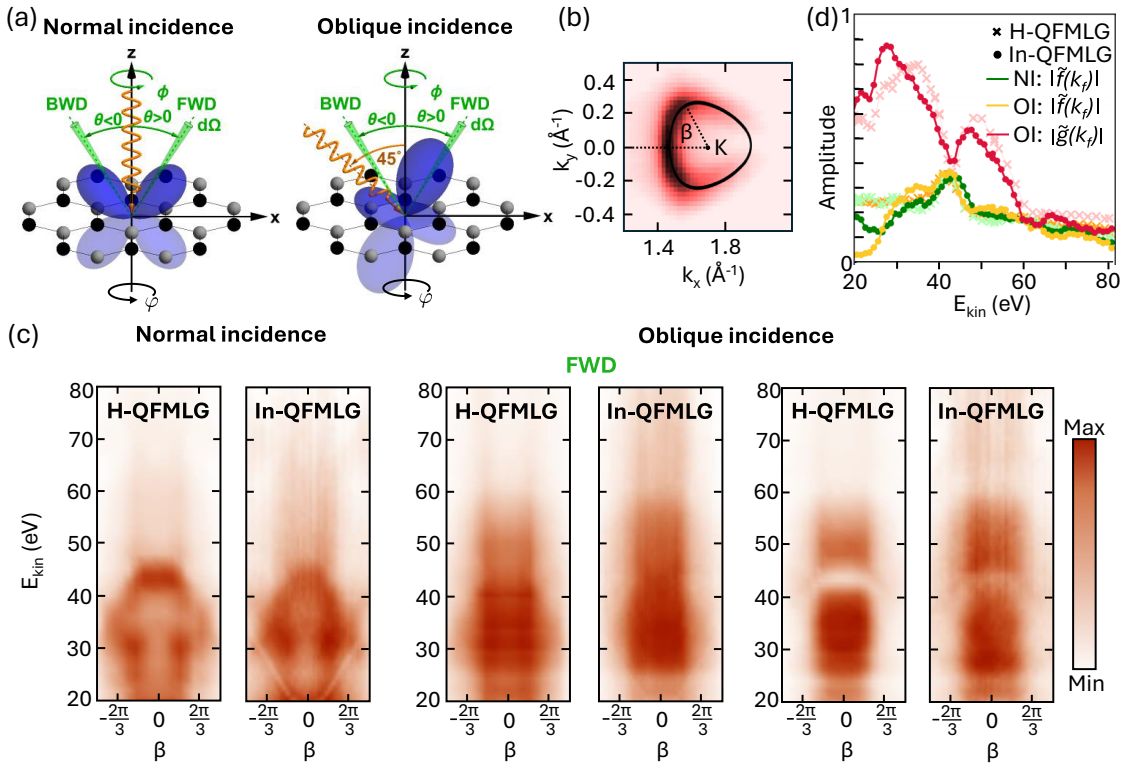

FIG. 1. Robustness of graphene's photoemission cross section. (a) NI geometry and OI geometry. The incident light polarization is shown by the yellow sine wave. Angle-resolved detection in $d\Omega$ around polar θ and azimuthal angle ϕ is illustrated in green. The blue lobes visualize the angular distributions of the pure d channel. In our experiment, only photoelectrons emitted into the (xz) plane, where $\phi = 0$, are detected. To obtain the momentum maps in panel (b), the sample is rotated around the z axis by varying φ. (b) Close-up of the typical horseshoe pattern arising in momentum maps close to the graphene K and K' points, recorded at initial-state energy 1.35 eV below the Dirac point at $E_{\rm kin} = 30$ eV. The panel additionally displays the contour (black line) and angle β along which the experimental data are plotted in panel (c). (c) Experimental photoemission intensities in three geometries as indicated, extracted along the black contour in panel (b) and compiled for densely sampled kinetic energies between 20 and 80 eV for H-QFMLG (left columns), as compared to In-QFMLG (right column). Note that here and below, the H-QFMLG experimental data are adapted from Ref. [21]. Intensities in each column are plotted to scale, with dark red corresponding to high intensity. Between the columns, the scaling is arbitrary. (d) Photoemission amplitudes $|\tilde{g}|$ and $|\tilde{f}|$ of s and d channels, respectively, extracted for H-QFMLG (crosses in light colors, [21]) and for In-QFMLG (circles in dark colors) as a function of final-state kinetic energy. The curves were extracted from experimental data at $\beta = 0$ in NI and OI geometries as indicated, using the SWA without nearest-neighbor scattering, assuming a constant phase shift $\Delta\sigma = 0$. See Ref. [21] for more details. The data in this figure were obtained at the MLS.

them to synchrotron facilities in air for further ARPES investigation [26].

Pristine indenene films (In/SiC—without a graphene layer) were prepared as previously described in Ref. [22], by inducing hydrogen desorption from the (1×1) SiC(0001) surface during indium deposition. This was achieved by heating the samples to 600 °C for 1 min while simultaneously exposing them to high-purity indium ($\geqslant$99.9999%) from a Knudsen cell maintained at 775 °C. The substrate temperature was measured using an optical pyrometer (Keller CellaTemp PA 20) with the emissivity set to 85%. The surface quality was verified after each step by low-energy electron diffraction.

B. ARPES measurements

Photon-energy-dependent ARPES cross-section measurements with calibrated photon flux were performed at the insertion-device beamline of the Metrology Light Source at the PTB in Germany, equipped with a toroidal electron analyzer [25,31]. The experiments were carried out with linear light polarization in both normal-incidence (NI) and oblique-incidence (OI) geometries, exactly following our procedure published in Ref. [21]. Most importantly, the calibrated photon beam intensity $I_{\rm ph}$ was determined from the continuously monitored beamline mirror current, gauged against the current of an absolutely calibrated semiconductor photodiode. Careful false-light suppression safeguarded that only photons with the right energy were counted. This resulted in photon-energy-dependent flux curves in units of photons per second per nanoampere of mirror current and allowed us to determine the differential photoemission cross section according to Eq. (C8) in Ref. [21]. Data on hydrogen-intercalated QFMLG on SiC (H-QFMLG) from these experiments are shown in Figs. 1, 7, and 11(c) and for In-QFMLG in Fig. 1.

Photon-energy-dependent CD-ARPES measurements on In-QFMLG reported in Figs. 3–5(b), and 8 were performed using the FOCUS NanoESCA momentum microscope at the Elettra Synchrotron in Trieste, Italy. Left and right circular

polarized light at $\alpha = 65^\circ$ incidence angle with respect to the sample surface normal was used, and the datasets were subtracted. Analogous CD-ARPES measurements were carried out on H-QFMLG samples [32], with the sample rotated by 30° relative to In-QFMLG, such that the incident light is aligned along the $K_{Gr}\Gamma K_{Gr}$ direction. Data from these experiments are shown in Figs. 3, 5(b), and 8.

Further, the intensity calibration results for pristine indenene in Figs. 6 and 12 were obtained with the microARPES instrument at the I05 beamline of Diamond Light Source in the UK, with the sample tilted by 6°, employing *p*-polarized light at an incidence angle of $\alpha = 50^\circ$ relative to the sample surface normal.

The CD-ARPES results of Fig. 9 were obtained with the microARPES instrument at the MAESTRO beamline of the Advanced Light Source (ALS) in the USA, employing a magic light-incidence angle of $\alpha = 54.7^\circ$ relative to the sample surface normal.

III. GRAPHENE AS AN ARPES INTENSITY STANDARD

To establish the π bands of QFMLG, i.e., graphene that is electronically decoupled from the substrate [24,26], as a quantitative intensity reference for ARPES, we demonstrate the following:

(1) The photoemission cross section of QFMLG's π bands is insensitive to sample quality and robust against external perturbations.

(2) A universal SWA model for QFMLG can be established, enabling the extraction of the phase of the photoemission matrix element from CD-ARPES.

(3) This model can be used to determine the QFMLG photoemission cross section in arbitrary experimental geometries and thus is able to serve as a reliable reference for intensity normalization across experimental configurations.

With these foundations, we finally employ QFMLG as a normalization standard to extract the photoemission cross section of the valence bands of a 2D test system—the quantum spin Hall insulator indenene [4,22,33].

A. Robustness of the photoemission cross section

To address point (1), we compare photoemission from H-QFMLG with a structurally distinct system—graphene intercalated by a triangular monolayer of indium, also known as indenene [4,22,26,33]. X-ray standing wave measurements show that, in both systems, graphene is van der Waals bonded to the intercalated layer and thus electronically decoupled [26,34]. Despite this similarity, the presence of heavy indium atoms in In-QFMLG is known to induce considerable photoelectron scattering [26]. Remarkably, we find that the photoemission cross section of the graphene overlayer remains essentially unaffected.

Previously reported ARPES data on H-QFMLG [21] were collected at the Metrology Light Source using a toroidal electron analyzer and normalized against the quantitatively calibrated photon flux [25,31]. Data were recorded under linearly polarized light for both NI (0°) and OI (45°), as illustrated in Fig. 1(a). In OI geometry, forward (FWD) and backward (BWD) emissions are no longer equivalent, yielding three linearly independent datasets.

The kinetic-energy-dependent ARPES intensity modulations around the graphene K point, forming the characteristic horseshoe in Fig. 1(b), are plotted as a function of the angular coordinate β in Fig. 1(c) (left panels). As discussed in detail in Ref. [21] and revisited in this work in Appendix A, these modulations are well described by applying the SWA to the graphene p_z tight-binding model, which accounts for final-state scattering in the on-site and nearest-neighbor potentials. Omitting nearest-neighbor scattering for the moment, the matrix elements for the conduction (−) and valence (+) bands of the Dirac cone take the form

$$M^{\pm}_{\boldsymbol{k}_f\boldsymbol{k}} \propto \frac{1}{\sqrt{2}}\boldsymbol{\epsilon}\cdot\left[(1 \pm e^{i\vartheta_{\boldsymbol{k}_f}})\boldsymbol{M}^{\eta\boldsymbol{k}_f}_{210}\right], \tag{2}$$

where $1 \pm e^{i\vartheta_{\boldsymbol{k}_f}}$ is the honeycomb structure factor and $\boldsymbol{M}^{\eta\boldsymbol{k}_f}_{210}$ encompasses dipole transitions from the C $2p_z$ ($\{n, l, m\} = \{2, 1, 0\}$) states into $l' = 0$ (*s* channel) and $l' = 2$ (*d* channel) photoemission orbits [18,21]:

$$\boldsymbol{M}^{\eta\boldsymbol{k}_f}_{210} = \underbrace{\widetilde{g}(k_f)\boldsymbol{Y}_{1,0,0}(\boldsymbol{\Omega}_{k_f})}_{s\text{ channel}} - \underbrace{\widetilde{f}(k_f)\boldsymbol{Y}_{1,2,0}(\boldsymbol{\Omega}_{k_f})}_{d\text{ channel}}. \tag{3}$$

The latter expression separates into two contributions: an angular part, governed by the vector spherical harmonics $\boldsymbol{Y}_{l,l',m}$ and analytically tractable; and a radial part, given by the amplitudes $|\widetilde{g}|$, $|\widetilde{f}|$ and the phase $\Delta\sigma = \arg(\widetilde{f}/\widetilde{g})$. The radial part depends sensitively on the photoelectron scattering potential (encoded in η [18]) and must be obtained either from advanced *ab initio* calculations or directly from experiment.

In Ref. [21], $|\widetilde{g}|$ and $|\widetilde{f}|$ have been extracted from the graphene data under the assumption of a constant phase $\Delta\sigma = 0$. These values, reproduced as light crosses in Fig. 1(d), serve as our baseline, to be compared both to the new data on In-QFMLG to which we now turn and to the more accurate reconstruction that we will present in Sec. III C.

Repeating the identical experimental and analytical procedure for In-QFMLG, we find that the horseshoe intensity modulations remain qualitatively unchanged [Fig. 1(c), right panels], and the extracted radial amplitudes [dark circles in Fig. 1(d)] are consistent with H-QFMLG. A singular value decomposition (SVD) analysis further confirms the robustness of this result against noise and sample imperfections (Appendix B). Furthermore, owing to its exceptional environmental stability, epitaxial graphene represents a particularly accessible platform for ARPES experiments, requiring only minimal sample handling after exposure to ambient conditions, typically limited to a mild outgassing step at approximately 150 °C for a few minutes [26]. We thus conclude that QFMLG is a reliable ARPES intensity reference.

B. Photoelectron phase extraction from CD-ARPES

The previous analysis assumed a zero phase shift ($\Delta\sigma = 0$) between the *s* and *d* photoemission channels. However, a realistic final-state scattering induces OAM and kinetic-energy-dependent phase shifts that in hydrogenlike atoms scale as $\arg[\Gamma(l + 1 + i\eta)]$, where $\eta = Z/(a_0 k_f)$ is the Sommerfeld parameter, and $k_f \propto \sqrt{E_{\text{kin}}}$ [18,21]. Although

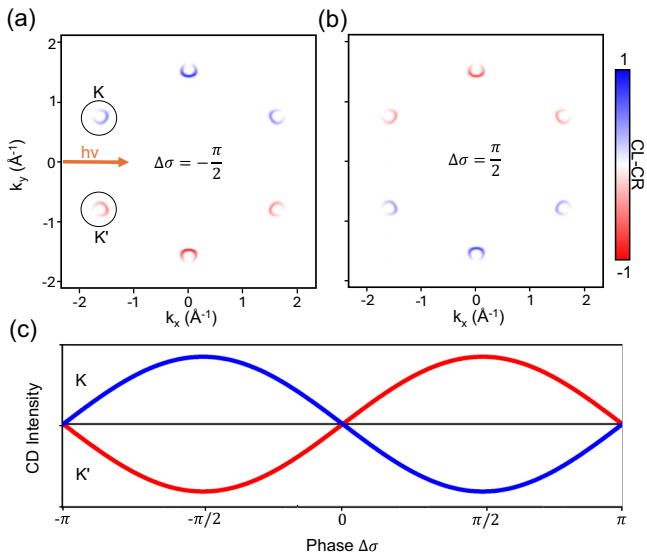

FIG. 2. Calculated geometric CD-ARPES of graphene. Constant-energy CD-ARPES maps of graphene, simulated 1 eV below the Dirac point within the simplified SWA, neglecting nearest-neighbor final-state scattering. The incident light is directed along the $M_{Gr}\Gamma M_{Gr}$ direction and tilted 65° from the surface normal. Panels (a) and (b) show the resulting circular-dichroism patterns for phase shifts of $\Delta\sigma = -\frac{\pi}{2}$ and $\Delta\sigma = \frac{\pi}{2}$, respectively, between the s and d photoemission channels. (c) Geometric CD asymmetry (see Appendix A) at the K and K′ points [highlighted in panel (a)], plotted as a function of $\Delta\sigma$, illustrating the phase-sensitive interference between the emission channels.

numerical calculations are typically required to estimate these phase shifts, in systems with few orbitals like graphene, $\Delta\sigma$ can be directly extracted from CD-ARPES [4,35].

According to Eqs. (2) and (3), an excitation of a p_z orbital by $\boldsymbol{\epsilon}$-polarized light results in photoemission with intensity given by $I_\epsilon \propto |\boldsymbol{\epsilon}\cdot\boldsymbol{M}_{210}^{\eta\boldsymbol{k}_f}|^2$, and the circular-dichroism asymmetry consequently reads $I_{\mathrm{CD}} = I_{\epsilon_{\circlearrowleft}} - I_{\epsilon_{\circlearrowright}}$. Given the out-of-plane angular momentum component of the p_z orbital is zero, I_{CD} vanishes by construction in NI geometry. In OI, however, the out-of-plane component of $\boldsymbol{\epsilon}$ mixes additional orbital contributions into the photoemission final state, producing the characteristic geometric CD asymmetry with respect to the light-incidence plane in Figs. 2(a) and 2(b), and making CD-ARPES sensitive to the phase shift $\Delta\sigma = \arg(\widetilde{f}/\widetilde{g})$ between photoemission s and d channels [18,21]: As shown in Fig. 2(c), the dichroic signal $I_{\mathrm{CD}} \propto \sin\Delta\sigma$ peaks when $\Delta\sigma$ is a half-integer multiple of π, but vanishes and switches sign at integer multiples of π.

Figure 3(a) presents CD-ARPES data 500 meV below the Dirac point of graphene of In-QFMLG recorded at $h\nu = 47$ eV. The characteristic horseshoe-shaped intensity distribution and the pronounced geometric CD asymmetry with respect to the light-incidence plane are clearly resolved. Comparable CD-ARPES patterns are found in H-QFMLG.

To quantify the dichroism, we integrate I_{CD} in the vicinity of the K and K′ points on both sides of the light-incidence plane and average the results for each intercalation system. The corresponding kinetic-energy dependence is shown in Fig. 3(b) [32] (see Appendix C for details). In both systems, three distinct sign reversals are observed. Notably, these occur at essentially identical kinetic energies of 32, 55, and 62 eV. Within our framework, these energies correspond to conditions where the relative phase shift $\Delta\sigma$ equals an integer multiple of π.

In Fig. 3(c), we show CD-ARPES band-structure maps along the $K_{Gr}M_{Gr}K'_{Gr}$ direction for three kinetic energies. Panels (i) and (iii) (42 and 85 eV) display the expected geometric CD asymmetry due to the orbital form factor (Appendix A), reflecting the handedness of the experimental geometry. Panel (ii), at 55 eV, reveals a suppressed geometric CD-ARPES background, but a nontrivial inversion of band contrast. Earlier polarization-dependent ARPES studies argued that momentum maps of the photoemission intensity can provide access to initial-state properties such as sublattice symmetry and isospin [36], electronic chirality and Berry phase [37], and the phase structure of the Bloch wavefunction [38]. Our results show, however, that polarization-dependent signatures in the momentum maps are not uniquely determined by the initial state: Final-state scattering can itself generate pronounced circular dichroism and characteristic intensity patterns in momentum space. Thus, wavefunction-sensitive interpretations of photoemission dichroism require the final-state contribution to be explicitly disentangled. In this context, we identify final-state dichroic scattering—the Daimon effect [32,39]—as a key contribution that can mimic signatures that might otherwise be attributed to initial-state pseudospin or Berry-phase effects.

This effect can be captured by extending our SWA model to include symmetry allowed nearest-neighbor scattering with OAM (Appendix A). The dipole matrix element then reads

$$M_{\boldsymbol{k}_f\boldsymbol{k}}^{\pm} \propto \frac{1}{\sqrt{2}}\boldsymbol{\epsilon}\cdot\Bigg[\underbrace{(1\pm e^{i\vartheta_{\boldsymbol{k}_f}})\boldsymbol{M}_{210}^{\eta\boldsymbol{k}_f}}_{\text{(I) horseshoe}} + \underbrace{\Sigma_0^{\pm}(\boldsymbol{k}_f)\sum_{j=2}^{\infty} a_j\boldsymbol{M}_{j10}^{\eta\boldsymbol{k}_f}}_{\text{(II) modulation}} + \underbrace{b\big(\Sigma_1^{\pm}(\boldsymbol{k}_f)\boldsymbol{M}_{321}^{\eta\boldsymbol{k}_f} - \Sigma_{-1}^{\pm}(\boldsymbol{k}_f)\boldsymbol{M}_{32-1}^{\eta\boldsymbol{k}_f}\big)}_{\text{(III) Daimon effect}}\Bigg], \tag{4}$$

where the $\Sigma_l^{\pm}$ are final-state structure factors for photoelectrons in orbits m. Here, term (II) incorporates nondichroic scattering into neighboring p_z orbitals already discussed in Ref. [21], while term (III) incorporates additional dichroic scattering into neighboring $3d$ orbitals ($\{n, l, m\} = \{3, 2, \pm 1\}$) that are sensitive to circular polarization. The small complex coefficients $a_j \equiv a_j(k_f)$ and $b \equiv b(k_f)$ encode the kinetic-energy dependence of final-state corrections. Notably, when $\Delta\sigma = 0$ or π, the dominant geometric CD-ARPES background vanishes, making the Daimon contribution experimentally visible—as confirmed by our measurements [Fig. 4(a)] and our model [Fig. 4(d)]. The model predicts that the Daimon asymmetry further switches sign across the Dirac point (see Appendixes A and C), an effect that is experimentally clearly confirmed in Figs. 4(b) and 4(c).

Having identified the kinetic energies where the phase shift $\Delta\sigma$ between s and d channel photoemission paths is an integer multiple of π and the geometric CD asymmetry reverses sign

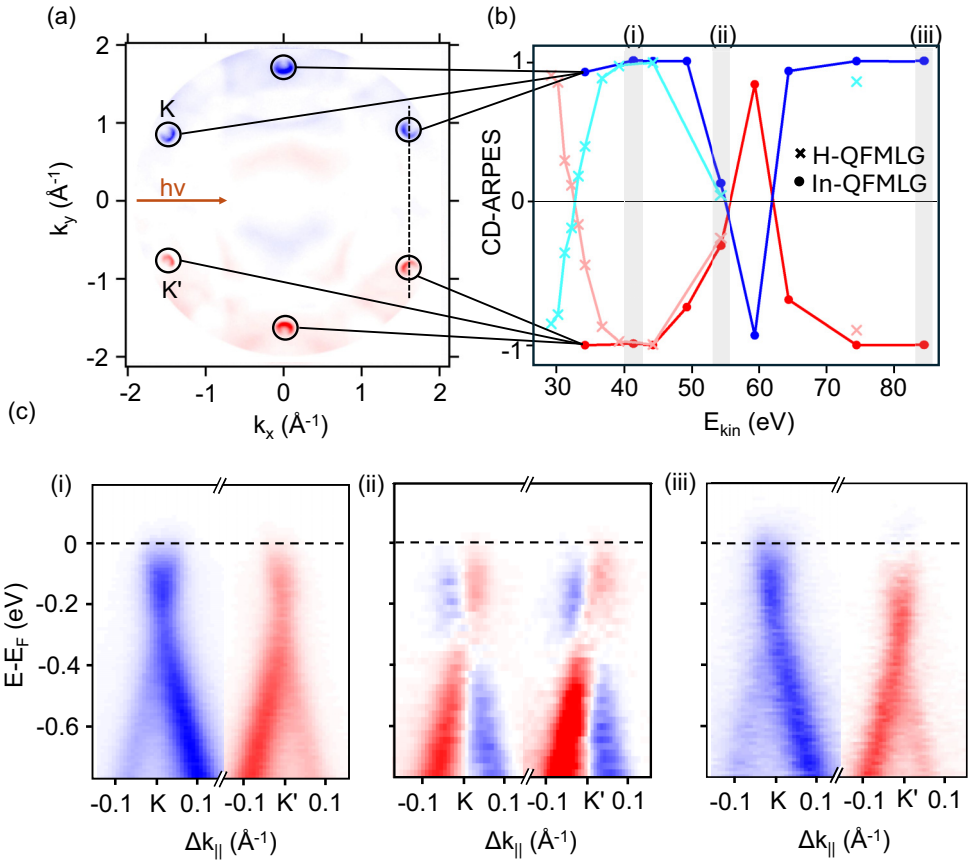

FIG. 3. Geometric CD asymmetry of the measured CD-ARPES of graphene. (a) CD-ARPES map of In-QFMLG measured at a photon energy of 47 eV with light incident at 65° along the $M_{Gr}\Gamma M_{Gr}$ direction 500 meV below the Dirac point of graphene. (b) Geometric CD asymmetry of In-QFMLG, integrated over a circular region of radius $k = 0.2$ Å^{-1} around the K and K′ points [highlighted in panel (a)], plotted as a function of kinetic energy E_{kin}. The intensities of the Dirac points on either side of the light-incidence plane were averaged. Dark circles correspond to measurements on In-QFMLG with light incidence along the $M_{Gr}\Gamma M_{Gr}$ direction; light crosses represent data reproduced from H-QFMLG with light incidence along the $K_{Gr}\Gamma K_{Gr}$ direction [32]. (c) CD-ARPES band-structure maps of In-QFMLG along the $K_{Gr}M_{Gr}K'_{Gr}$ high-symmetry path, shown as a dashed line in panel (a), measured at photon energies of (i) 47 eV, (ii) 60 eV, and (iii) 90 eV. Panels (i) and (iii) display the geometric CD asymmetry with respect to the light-incidence direction, while in panel (ii), this asymmetry is suppressed and replaced by the Daimon effect, attributed to dichroic final-state scattering. The data in this figure were obtained at Elettra.

[Fig. 3(b), reproduced in Fig. 5(b)], we can finally reconstruct the phase profile $\Delta\sigma \mod \pi$ in Fig. 5(a). This reconstruction assumes a continuous evolution of $\Delta\sigma$ with kinetic energy. While the hydrogenlike $2p$ orbital model predicts an approximately linear phase evolution between successive integer multiples of π (see Appendix D), we tested the validity of this assumption by introducing sinusoidal variations of $\Delta\sigma$ between the experimentally constrained phase points and assessing their influence on the reconstructed amplitudes. This phase profile replaces the simplified assumption of a constant phase (i.e., $\Delta\sigma = 0$) and allows us to reconstruct more accurately the radial dipole amplitudes $|\widetilde{g}(k_f)|$ and $|\widetilde{f}(k_f)|$ in the next section.

C. Radial cross section in graphene

Having confirmed the validity of the SWA-based model of photoemission through experimental results for two different graphene-based systems and after reconstruction of the kinetic-energy-dependent phase profile, we now aim to fully reconstruct the energy-dependent photoemission cross section of graphene's Dirac bands.

Using the procedure outlined in Ref. [21], which was previously applied to reconstruct the radial dipole amplitudes $|\widetilde{g}(k_f)|$ and $|\widetilde{f}(k_f)|$ in Fig. 1(d) under the assumption of an artificially constant phase shift $\Delta\sigma = 0$, we now refine the analysis by incorporating the experimentally determined phase profile shown in Fig. 5(a). This enables a more accurate reconstruction of the radial dipole amplitudes.

The resulting amplitudes $|\widetilde{g}(k_f)|$ and $|\widetilde{f}(k_f)|$ are displayed as a function of kinetic energy in Fig. 5(c) and provided—along with $\Delta\sigma$—on the WueData repository for reference [40]. Importantly, while the amplitudes are highly sensitive to the precise energy positions of the mod-π nodes, they remain remarkably robust against deviations of the phase evolution between these nodes (shaded contour).

Qualitatively, our results align with calculations of the radial dipole matrix elements for a hydrogenlike $2p_z$ orbital (see Appendix D). Notably, both exhibit a pronounced node (Cooper minimum [41]) in the s channel amplitude $|\widetilde{g}(k_f)|$,

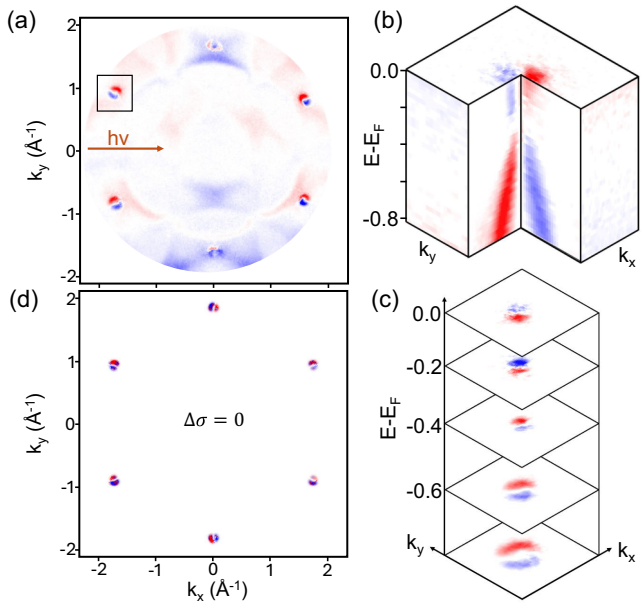

FIG. 4. Daimon effect in graphene. (a) Constant-energy CD-ARPES map of In-QFMLG, measured at Elettra at a photon energy of 60 eV with light incident at 65° along the $M_{Gr}\Gamma M_{Gr}$ direction 500 meV below the Dirac point. At this energy, the geometric CD asymmetry is suppressed, revealing the Daimon effect arising from dichroic final-state scattering. (b) Three-dimensional k_x, k_y, E_{bin} rendering of the CD-ARPES signal, corresponding to the region highlighted by the black square in panel (a). (c) Binding-energy-resolved sequence of constant-energy CD-ARPES slices, illustrating the change across the valence band due to the Daimon effect. (d) Simulated CD-ARPES constant-energy map of graphene based on the SWA model, including nearest-neighbor final-state scattering and a phase shift of $\Delta\sigma = 0$. The simulation qualitatively reproduces features of the experimentally observed Daimon effect, as expected because of the E_{kin} dependence of $\Delta\sigma$ for graphene as displayed in Fig. 5 and the behavior of $\Delta\sigma$ shown in Fig. 2(c).

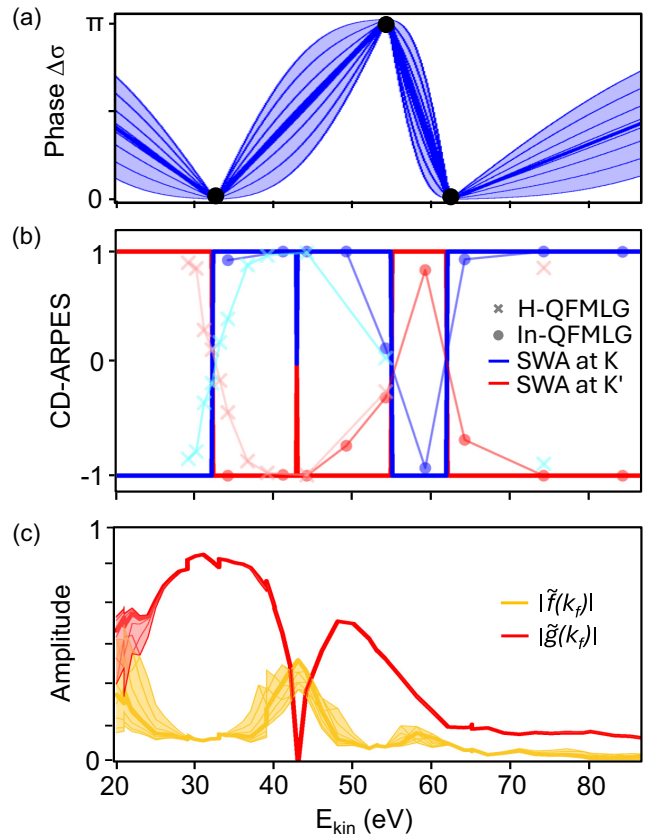

FIG. 5. Radial photoemission cross section of graphene. (a) Kinetic-energy-dependent phase profiles $\Delta\sigma$, reconstructed experimentally under the assumption of a linear and sinusoidal interpolation (blue) between the experimentally determined phase-flip points (black) extracted from the CD-ARPES asymmetry. (b) The red and blue solid lines represent the corresponding SWA model calculations, parametrized using the amplitude functions $|\tilde{g}(k_f)|$ and $|\tilde{f}(k_f)|$ of the s and d channels, extracted in panel (c), and the relative phase profile $\Delta\sigma$ derived from the CD-ARPES data shown in panel (a). Data points showing the geometric CD asymmetry of graphene, reproduced from Fig. 3(b), are shown in a lighter shade. (c) Radial dipole amplitudes $|\tilde{g}(k_f)|$ and $|\tilde{f}(k_f)|$ corresponding to the s and d photoemission channels of graphene, extracted from the NI, FWD, and BWD datasets in Fig. 1, using the SWA model without final-state scattering and employing the phase profile from panel (a). The shaded area indicates the estimated spread due to the uncertainty of the phase between the fixed points at 0 and π revealed by experiments (see Appendix D).

while the d channel amplitude $|\tilde{f}(k_f)|$ displays a broad maximum at the same energy, lacking such a node. However, significant quantitative deviations are evident, highlighting the influence of the solid-state environment on the photoemission process—departing markedly from the idealized hydrogenlike case. These deviations underline the importance of experimentally normalized matrix elements in solid-state systems.

To validate the internal consistency of our model, we reintegrate the extracted amplitudes and phases into the SWA model of Eq. (2) and compute the circular dichroism around all graphene K and K′ points as a function of kinetic energy E_{kin}. The calculated sign of the geometric CD asymmetry, shown in Fig. 5(b), is in good agreement with experimental measurements, confirming the self-consistency of our reconstruction.

Interestingly, the model further predicts a vanishing geometric CD-ARPES signal at a kinetic energy of approximately 43 eV [see Fig. 5(b)]. Unlike other minima in the dichroism spectrum, no sign reversal occurs here. This is because, at this energy, the s channel exhibits a Cooper minimum where the amplitude $|\tilde{g}(k_f)|$ is suppressed entirely [see Fig. 5(c)], eliminating interference with the d channel—the origin of the geometric CD-ARPES effect.

IV. APPLICATION TO A QSHI

With the SWA model fully established and experimentally calibrated for the graphene π bands, we now demonstrate its capability as an intensity reference in a representative setting. Specifically, we employ QFMLG as an *in situ* intensity reference to normalize the photoemission signal from another material under realistic experimental conditions. The central idea is straightforward: A band of interest can be referenced against QFMLG—either as part of the sample or as a separate

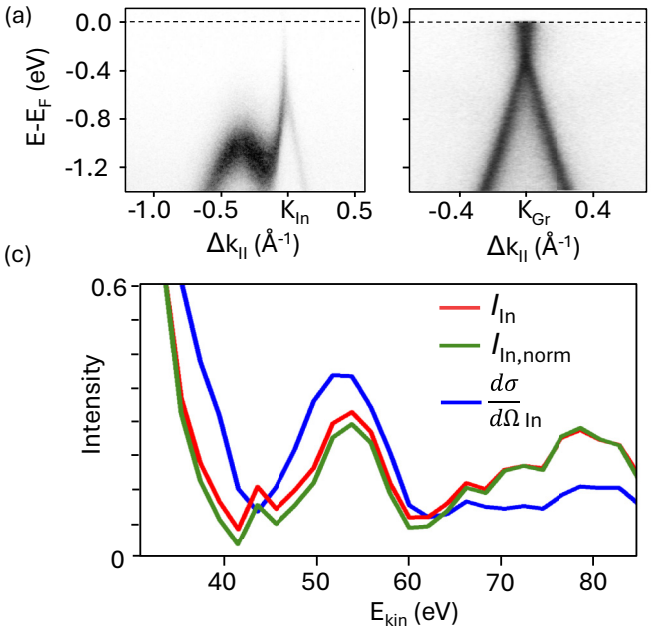

FIG. 6. ARPES cross section of the indenene valence band. (a) ARPES band dispersion centered at the indenene K point (K_{In}). (b) Corresponding dispersion centered at the graphene K point (K_{Gr}). Both datasets were recorded at Diamond Light Source, using 50° light incidence along the $K_{Gr}\Gamma K'_{Gr}$ direction. (c) Uncorrected photoemission intensity of the indenene valence band as a function of kinetic energy (red), corresponding drain current corrected intensity (green), and extracted differential photoemission cross section (blue).

sample—measured independently under identical photon energy and geometrical configuration. This procedure provides a framework for quantitative intensity scaling of a target system without requiring an independently characterized light source or detector, assuming that residual instrumental effects are minor, as discussed in Sec. V.

As a test case, we again investigate the quantum spin Hall insulator indenene [4,22,26,33], but this time the pristine phase without graphene on top, using microARPES at the I05 beamline of the Diamond Light Source. The ARPES map shown in Fig. 6(a) clearly displays its Dirac features. The Dirac bands of graphene from a separate H-QFMLG sample measured independently under identical experimental conditions in Fig. 6(b) serve as an intrinsic intensity reference, while the indenene valence band in Fig. 6(a) constitutes the target for intensity normalization.

We record the graphene ARPES intensity I_{Gr} at the K point over kinetic energies between 30 and 85 eV, using horizontally oriented linear polarization at an incidence angle of 50°. According to Eq. (1), the measured intensity is proportional to the analyzer detection efficiency $\chi(k_f)$, the photon flux $I_{ph}(h\nu, \boldsymbol{\epsilon})$, and the differential photoemission cross section $\frac{d\sigma}{d\Omega}(k_f, \Omega_{\boldsymbol{k}_f}; h\nu, \boldsymbol{\epsilon})$ [21], the latter of which is proportional to the modulus squared of the dipole transition matrix element $\frac{d\sigma}{d\Omega}(k_f, \Omega_{\boldsymbol{k}_f}; h\nu, \boldsymbol{\epsilon}) \propto |M^{\pm}_{\boldsymbol{k}_f\boldsymbol{k}}|^2$.

Within the SWA framework [Eq. (2)], and using the previously determined parameters $|\widetilde{g}|$, $|\widetilde{f}|$, and $\Delta\sigma$ in Figs. 5(a) and 5(c), the graphene cross section $\frac{d\sigma}{d\Omega}_{Gr}(k_f, \Omega_{\boldsymbol{k}_f}; h\nu, \boldsymbol{\epsilon})$ can be calculated explicitly for the given experimental setting using Eqs. (2) and (3). Dividing the measured graphene intensity by the corresponding calculated cross section yields $\chi(k_f)I_{ph}(h\nu, \boldsymbol{\epsilon})$, the product of beamline flux and detector response. This quantity can subsequently be used to correct the intensity of any other band measured under identical experimental conditions for instrumental and geometrical effects (see Appendix E).

Applying this protocol, we extract the kinetic-energy-dependent photoemission cross section of the pristine indenene valence band $\frac{d\sigma}{d\Omega}_{In}(k_f, \Omega_{\boldsymbol{k}_f}; h\nu, \boldsymbol{\epsilon})$ up to an overall constant factor, as shown in Fig. 6(c). Comparing it to the uncorrected intensity, as well as to intensity corrected by the drain current of a beamline optical element, we find marked qualitative differences with respect to $\frac{d\sigma}{d\Omega}_{In}$. This example illustrates how graphene can serve as a transferable, geometry-matched reference standard for quantitative ARPES intensity calibration across different materials and experimental platforms.

V. IMPLICATIONS, LIMITATIONS, AND OUTLOOK

Our results establish that even for a paradigmatic few-band system, such as graphene, the ARPES intensity cannot be interpreted as a direct map of the initial-state electronic structure alone. Instead, it reflects the coherent superposition of initial-state orbital character and final-state scattering. By systematically varying the geometry and light polarization and fitting the data within a minimal scattered-wave ansatz, we show that the full complex dipole matrix element can be reconstructed experimentally in a channel-resolved fashion. The pronounced deviations from hydrogenic cross sections—anticipated neither by oversimplified tight-binding approaches nor by realistic density-functional calculations (see Appendix D)—identify the solid-state environment as an active and nontrivial constituent of the photoemission process. More broadly, our findings highlight the importance of accounting for final-state and phase effects in ARPES-based approaches aimed at reconstructing molecular orbitals [2,7,15], orbital angular momenta [4], Berry curvature [5], or the quantum-geometric tensor [6], particularly in multiband systems.

Beyond this conceptual advance, we establish QFMLG as a transferable intensity standard for ARPES. Referencing to graphene enables quantitative correction of photoemission intensities for photon flux and detector response directly at the sample position, without auxiliary flux monitors that are susceptible to false-light contributions. This protocol provides direct access to kinetic-energy-resolved differential cross sections, independent of beamline configuration and fully taking into account the experimental geometry.

The accuracy of such a calibration, however, relies critically on maintaining identical measurement geometries, as deviations in sample alignment, sample height or tilt, analyzer lens settings, or beam footprint can modify the measured intensity distribution. For this reason, the graphene reference should ideally be measured immediately before the sample of interest under otherwise unchanged experimental conditions, thereby minimizing changes in analyzer transmission and photoelectron optics. Further, while modern synchrotron

beamlines routinely provide linear polarization purities close to 100%, residual deviations can introduce systematic uncertainties [42]. Such effects, however, can be quantified independently through polarization-sensitive reference measurements, for example, by exploiting the well-established polarization dependence of Shockley surface states of noble-metal surfaces [43].

Taking these sources of experimental uncertainty into account, and considering the widespread availability and stability of high-quality QFMLG, the strategy introduced in this article offers a scalable route toward reproducible intensity normalization across experimental (synchrotron) facilities. More broadly, it suggests a framework in which quantum materials themselves can serve as intrinsic reference standards, thereby expanding the quantitative capabilities of photoemission spectroscopy for wavefunction-sensitive measurements.

ACKNOWLEDGMENTS

We thank A. Haags, L. Egger, X. Yang, S. Wolff, T. Seyller, M. Richter, M. G. Ramsey, and F. C. Bocquet for their contributions to the experimental data on H-QFMLG, which are discussed in detail in Ref. [21] and were partly used in this work. We are grateful for funding support from the Deutsche Forschungsgemeinschaft (DFG, German Research Foundation) under Germany's Excellence Strategy through the Würzburg-Dresden Cluster of Excellence on Complexity, Topology and Dynamics in Quantum Matter ctd.qmat (EXC 2147, Project No. 390858490), and through the Collaborative Research Center SFB 1170 ToCoTronics (Project No. 258499086). We thank Physikalisch-Technische Bundesanstalt for time at the Metrology Light Source, the Diamond Light Source for time at beamline I05 (proposal SI40195), the Elettra-Sincrotrone Trieste for time at NanoESCA (proposal 20205032), and the Advanced Light Source, a U.S. DOE Office of Science User Facility under Contract No. DE-AC02-05CH11231. We further thank J. Riley (La Trobe University, Australia) and H. Kaser (Physikalisch-Technische Bundesanstalt, Germany) for experimental support. We acknowledge support by the European Union through the Synergy Grant Orbital Cinema (101071259) by the European Research Council (ERC), and from the Deutsche Forschungsgemeinschaft under Germany' Excellence Strategy through the Cluster of Excellence Matter and Light for Quantum Computing ML4Q (EXC 2004, Project No. 390534769).

C.S. grew indenene/SiC and In-QFMLG samples. Experiments with In-QFMLG on the MLS beamline were conducted by C.S., S.S., S.M., H.K., and A.G., while the circular-dichroism measurements were carried out at Elettra and the ALS by C.S., J.E., L.G., P.K., K.S., M.S., B.L., V.F., C.J., A.B., E.R., L.P., and S.M. Additional measurements were performed at Diamond by C.S., L.G., K.S., T.K., and C.C. The DFT calculations were performed by S.E. C.S. performed the data analysis. S.M. developed the model, guided the project, and wrote the manuscript with contributions from all authors. Funding for the experimental research was provided by A.G., F.S.T., R.C., and S.M.

The authors declare no competing interests.

DATA AVAILABILITY

The data that support the findings of this article are openly available [40].

APPENDIX A: PHOTOEMISSION FROM π BANDS OF GRAPHENE INCLUDING NEAREST-NEIGHBOR SCATTERING

An analytic form of the cross section of photoemission from the π bands of graphene including nearest-neighbor final-state scattering was developed in detail in Ref. [21]. Let us resume this discussion starting from its Eq. (F28):

$$M^{\pm}_{\boldsymbol{k}_f\boldsymbol{k}} \propto \frac{1}{\sqrt{2}}\boldsymbol{\epsilon}\cdot\Bigg[(1\pm e^{i\vartheta_{\boldsymbol{k}_f}})\boldsymbol{M}^{\eta\boldsymbol{k}_f}_{210} + \sum_{nlm} S^{nlm}_{210}(\boldsymbol{n}_0)\boldsymbol{M}^{\eta\boldsymbol{k}_f}_{nlm} \times \sum_{j=0}^{2} e^{-i\pi\frac{2j}{3}m}\Big(e^{-i\boldsymbol{k}_f\cdot\boldsymbol{n}_j} \pm e^{i\vartheta_{\boldsymbol{k}_f}} e^{-i\pi m} e^{i\boldsymbol{k}_f\cdot\boldsymbol{n}_j}\Big)\Bigg],$$

where the index $j = 0\cdots 2$ labels the vectors $\boldsymbol{n}_j$ connecting atoms of sublattice A with their three nearest neighbors on sublattice B, and $\vartheta_{\boldsymbol{k}_f} = \arg\sum_{j=0}^{2} e^{i\boldsymbol{n}_j\cdot\boldsymbol{k}}$ measures the geometric phase associated with the corresponding structure factor $1\pm e^{i\vartheta_{\boldsymbol{k}_f}}$ [1]. The photoemission matrix elements $\boldsymbol{M}^{\eta\boldsymbol{k}_f}_{nlm}$ describe the dipole cross sections of atomic orbitals with quantum numbers $\{nlm\}$ in the basis of the light polarization vector $\boldsymbol{\epsilon}$. Their calculation is detailed in Refs. [18,21]. The dimensionless Sommerfeld parameter $\eta = Z/(a_0 k_f)$ hereby describes the distortion of the outgoing photoelectron wave with wave vector k_f in the Coulomb field produced by the effective charge Z of the ion that it leaves behind. a_0 is the Bohr radius. Note that the Sommerfeld parameter takes the role of the principal quantum number n that characterizes bound state atomic orbitals.

The Shibuya-Wulfman integrals S^{nlm}_{210} are necessary to describe nearest-neighbor final-state scattering: They can be calculated analytically, e.g., via Eq. (78) in Ref. [44]:

$$S^{nlm}_{210}(\boldsymbol{n}_j) \propto \sum_{N,L}\sqrt{6nN(2l+1)}\langle l,-m;1,0|L,-m\rangle f_{NL}(n_j)Y^{-m}_{L}(\boldsymbol{\Omega}_{n_j}). \tag{A1}$$

Effectively, the Shibuya-Wulfman integrals perform a basis change between a C $2p_z$ orbital centered on sublattice A of graphene and a linear combination of atomic orbitals $\{nlm\}$ centered on nearest-neighbor C atoms on sublattice B, and vice versa [44,45]. In other words, they describe the $\{nlm\}$ orbital character of a C $2p_z$ orbital sitting on a neighboring site. The radial contributions f_{NL} to S^{nlm}_{210} decay exponentially with orbital distance, i.e., $f_{NL} \propto e^{-\alpha|\boldsymbol{n}_j|/2} = e^{-\frac{Z}{a_0 n}|\boldsymbol{n}_j|}$ with effective nuclear charge Z and Bohr radius a_0, where $|\boldsymbol{n}_j|$ in our nearest-neighbor model is equivalent to the sublattice distance $n_j = 1.421$ Å. This exponential decay justifies our nearest-neighbor final-state scattering approximation.

Making use of the fact that the angular components Y^{-m}_{L} in Eq. (A1) transform as $C^j_\nu Y^{-m}_{L} = e^{-i2\pi/\nu jm}Y^{-m}_{L}$ under ν-fold rotation C_ν, we find $S^{nlm}_{210}(\boldsymbol{n}_j) = C^j_3 S^{nlm}_{210}(\boldsymbol{n}_0) = e^{-i\pi\frac{2j}{3}m}S^{nlm}_{210}(\boldsymbol{n}_0)$ and $S^{nlm}_{210}(-\boldsymbol{n}_0) = C_2 S^{nlm}_{210}(\boldsymbol{n}_0) = e^{-i\pi m}S^{nlm}_{210}(\boldsymbol{n}_0)$. Further, since the C $2p_z$ orbital possesses

a node in the graphene xy plane and the vectors $\boldsymbol{n}_j$ connecting the two sublattices A and B lie within this plane, S_{210}^{nlm} are necessarily zero for $l+m=0 \mod 2$, i.e., for all orbitals l, m for which the xy plane is not a nodal plane.

Finally, for photoelectrons from C $2p_z$ orbitals to effectively get scattered into orbits of angular momentum l at adjacent sites, they must overcome the centrifugal barrier, i.e., $k_f^2 \geqslant l(l+1)/a^2$, where a is the atomic radius. With $a_{\text{carbon}} \sim 0.7$ Å and $k_f^{\max} \leqslant 5$ Å^{-1} for ARPES performed below 100 eV kinetic energy, this criterion suggests that channels with $l < 3$ may contribute. However, since the lowest-order contributions capable of capturing the essential physics of the Daimon effect in graphene arise from orbitals with $l \leqslant 2$, we restrict our consideration to these channels for simplicity. The corresponding contributions arise from $\{n, l, m\} = \{2, 1, 0\}$, $\{3, 1, 0\}$ and $\{3, 2, \pm 1\}$, allowing us to approximate

$$
\begin{aligned}
M^{\pm}_{\boldsymbol{k}_f\boldsymbol{k}} &\propto \frac{1}{\sqrt{2}}\boldsymbol{\epsilon}\cdot\Bigg[(1\pm e^{i\vartheta_{\boldsymbol{k}_f}})\boldsymbol{M}_{210}^{\eta\boldsymbol{k}_f} + \left(S_{210}^{210}(\boldsymbol{n}_0)\boldsymbol{M}_{210}^{\eta\boldsymbol{k}_f} + S_{210}^{310}(\boldsymbol{n}_0)\boldsymbol{M}_{310}^{\eta\boldsymbol{k}_f}\right)\sum_{j=0}^{2}(e^{-i\boldsymbol{k}_f\cdot\boldsymbol{n}_j} \pm e^{i\vartheta_{\boldsymbol{k}_f}}e^{i\boldsymbol{k}_f\cdot\boldsymbol{n}_j}) \\
&\quad + S_{210}^{321}(\boldsymbol{n}_0)\boldsymbol{M}_{321}^{\eta\boldsymbol{k}_f}\sum_{j=0}^{2}e^{-i\pi\frac{2j}{3}}(e^{-i\boldsymbol{k}_f\cdot\boldsymbol{n}_j} \pm e^{i\vartheta_{\boldsymbol{k}_f}}e^{-i\pi}e^{i\boldsymbol{k}_f\cdot\boldsymbol{n}_j}) + S_{210}^{32-1}(\boldsymbol{n}_0)\boldsymbol{M}_{32-1}^{\eta\boldsymbol{k}_f}\sum_{j=0}^{2}e^{i\pi\frac{2j}{3}}(e^{-i\boldsymbol{k}_f\cdot\boldsymbol{n}_j} \pm e^{i\vartheta_{\boldsymbol{k}_f}}e^{i\pi}e^{i\boldsymbol{k}_f\cdot\boldsymbol{n}_j})\Bigg] \\
&= \frac{1}{\sqrt{2}}\boldsymbol{\epsilon}\cdot\Bigg[\underbrace{(1\pm e^{i\vartheta_{\boldsymbol{k}_f}})\boldsymbol{M}_{210}^{\eta\boldsymbol{k}_f}}_{\text{horseshoe}} + \underbrace{\Sigma_0^{\pm}(\boldsymbol{k}_f)\left(S_{210}^{210}(\boldsymbol{n}_0)\boldsymbol{M}_{210}^{\eta\boldsymbol{k}_f} + S_{210}^{310}(\boldsymbol{n}_0)\boldsymbol{M}_{310}^{\eta\boldsymbol{k}_f}\right)}_{\text{signal modulation within horseshoe}} + \underbrace{\Sigma_1^{\pm}(\boldsymbol{k}_f)S_{210}^{321}(\boldsymbol{n}_0)\boldsymbol{M}_{321}^{\eta\boldsymbol{k}_f} + \Sigma_{-1}^{\pm}(\boldsymbol{k}_f)S_{210}^{32-1}(\boldsymbol{n}_0)\boldsymbol{M}_{32-1}^{\eta\boldsymbol{k}_f}}_{\text{circular dichroism of horseshoe due to final-state scattering}}\Bigg].
\end{aligned}
\tag{A2}
$$

We thus expect three contributions to the ARPES intensity distribution $I(\boldsymbol{k}_f) \propto |M_{\boldsymbol{k}_f\boldsymbol{k}}|^2$ of graphene's π bands described below.

1. The structure factor

The first term in the square brackets of Eq. (A2) contains the structure factor of the graphene lattice and produces a photoemission intensity that is proportional to $|\frac{1}{\sqrt{2}}(1\pm e^{i\vartheta_{\boldsymbol{k}}})|^2 = 1\pm\cos\vartheta_{\boldsymbol{k}}$ that gives rise to the conventional horseshoe pattern of its π bands, seen, for example, in Fig. 1(b). This horseshoe reflects the interference of partial waves emerging from sublattice sites A and B. Importantly, we note that the structure factor $1\pm\cos\vartheta_{\boldsymbol{k}}$ is already well described by the plane-wave final-state approximation $\eta \to 0$ that was discussed in detail in Ref. [1].

2. The orbital form factor

The structure factor in Eq. (A2) is multiplied by the dipole transition matrix element $\boldsymbol{M}_{210}^{\eta\boldsymbol{k}_f}$, which describes the angle-dependent, i.e., $\boldsymbol{k}_f$-dependent, cross section of the C $2p_z$ orbitals and is given by Eq. (F19) in Ref. [21]:

$$
\boldsymbol{\epsilon}\boldsymbol{M}_{210}^{\eta\boldsymbol{k}_f} = \underbrace{-\widetilde{f}(k_f)\left(\sqrt{\tfrac{3}{10}}\varepsilon_{\circlearrowright}Y_2^1(\boldsymbol{\Omega}_{k_f}) - \sqrt{\tfrac{2}{5}}\epsilon_0 Y_2^0(\boldsymbol{\Omega}_{k_f}) + \sqrt{\tfrac{3}{10}}\varepsilon_{\circlearrowleft}Y_2^{-1}(\boldsymbol{\Omega}_{k_f})\right)}_{d\text{ channel}} + \underbrace{\widetilde{g}(k_f)\,\epsilon_0 Y_0^0(\boldsymbol{\Omega}_{k_f})}_{s\text{ channel}}.
$$

This term thus accounts for the k_f-dependent interference between s and d channels discussed in detail in Refs. [1,21], and clearly goes beyond the plane-wave approximation discussed in Ref. [1]: If the light polarization is oriented purely in-plane with respect to the graphene lattice, e.g., if the ARPES experiment operates at NI and the out-of-plane polarization component $\epsilon_0 = 0$, then the s channel is suppressed, and ARPES becomes a k_f-dependent measure of the absolute d channel's cross section $|\widetilde{f}(k_f)|$. The complementary cross section of the s channel $|\widetilde{g}(k_f)|$ can then be reconstructed from the interference pattern obtained with mixed polarization in an oblique incidence geometry. Indeed, we have shown in Ref. [21] that if tunable light with calibrated photon flux—as provided by the Metrology Light Source of the Physikalisch Technische Bundesanstalt in Berlin—is available, one can exploit this to obtain quantitative information about radial cross sections of graphene (see Fig. 3 in Ref. [21]).

Further, it is important to note that in normal-incidence geometry, when $\epsilon_0 = 0$, a switch from right circular $\epsilon_{\circlearrowright}$ to left circular polarized light $\epsilon_{\circlearrowleft}$ does not change the modulus square of $|\boldsymbol{M}_{210}^{\eta\boldsymbol{k}_f}|^2$. This term is thus incapable of producing circular dichroism in ARPES if the polarization state is pure—unsurprising given that it describes photoelectrons from orbits with magnetic quantum number $m = 0$. Even in an oblique light incidence, this term will only generate a geometric CD asymmetry with respect to the scattering plane that is discussed in detail in Refs. [1,18], thereby reflecting the handedness of the photoemission experiment generated by light incidence, surface normal, and photoelectron momentum.

Finally, we note that in the plane-wave final-state approximation, $\boldsymbol{M}_{210}^{\eta\boldsymbol{k}_f}$ would be simply replaced by $\boldsymbol{k}_f\cdot\widetilde{p}_z(\boldsymbol{k}_f)$ [1]. In other words, this term would then contain the Fourier transform of the real space orbital and thus encode the shape of the p_z orbitals that build the initial-state Bloch wave. In

analogy to the form factor known from kinematic scattering theory, we then identify this term as an orbital form factor. In this simplistic picture, there would thus be a one-to-one relationship between ARPES intensity distributions and the shape of an orbital, i.e., the Wannier orbital within the unit cell of a crystal or the molecular orbital within a confined structure.

a. Nondichroic final-state scattering

The second term in the square brackets of Eq. (A2) goes beyond the kinematic approximation and represents scattering of the outgoing photoelectron wave into nearest-neighbor orbits of likewise zero OAM $m = 0$. This term scales with the $\boldsymbol{k}_f$-dependent final-state structure factor $\Sigma_0^{\pm} = \sum_{j=0}^{2}(e^{-i\boldsymbol{k}_f\cdot\boldsymbol{n}_j} \pm e^{i\vartheta_{\boldsymbol{k}_f}} e^{i\boldsymbol{k}_f\cdot\boldsymbol{n}_j}) \propto e^{-i\vartheta_{\boldsymbol{k}_{f\parallel}}} \pm e^{i2\vartheta_{\boldsymbol{k}_{f\parallel}}}$ that reflects photoelectrons emanating from sublattice A to scatter at the three sites of the adjacent sublattice B, and vice versa, and produces a minor correction to the ARPES intensity that redistributes spectral weight within the horseshoe feature. This redistribution has been experimentally demonstrated and discussed in detail in Ref. [21]. As the scattering states reflected in the corresponding dipole transition matrices $\boldsymbol{M}_{210}^{\eta\boldsymbol{k}_f}$ and $\boldsymbol{M}_{310}^{\eta\boldsymbol{k}_f}$ do not carry any OAM $m = 0$, they are again incapable of producing nontrivial, i.e., intrinsic circular dichroism, if the polarization state is pure.

b. Dichroic final-state scattering

Finally, introducing $\Sigma_{\pm 1}^{\pm}(\boldsymbol{k}_f) = \sum_{j=0}^{2} e^{\mp i\pi\frac{2j}{3}}(e^{-i\boldsymbol{k}_f\cdot\boldsymbol{n}_j} \pm e^{i\vartheta_{\boldsymbol{k}_f}} e^{\mp i\pi} e^{i\boldsymbol{k}_f\cdot\boldsymbol{n}_j})$ and exploiting the identities $S_{210}^{32-1}(\boldsymbol{n}_0) = -S_{210}^{321}(\boldsymbol{n}_0)$ and $|\Sigma_{-1}^{\pm}(\boldsymbol{k}_f)| = |\Sigma_{1}^{\pm}(\boldsymbol{k}_f)|$, we can simplify the third term in the square brackets of Eq. (A2) and obtain

$$S_{210}^{321}(\boldsymbol{n}_0)\boldsymbol{M}_{321}^{\eta\boldsymbol{k}_f}\Sigma_1^{\pm}(\boldsymbol{k}_f) + S_{210}^{32-1}(\boldsymbol{n}_0)\boldsymbol{M}_{32-1}^{\eta\boldsymbol{k}_f}\Sigma_{-1}^{\pm}(\boldsymbol{k}_f) = S_{210}^{321}(\boldsymbol{n}_0)\Sigma_1^{\pm}(\boldsymbol{k}_f)\big(\boldsymbol{M}_{321}^{\eta\boldsymbol{k}_f} - e^{i\zeta(\boldsymbol{k}_f)}\boldsymbol{M}_{32-1}^{\eta\boldsymbol{k}_f}\big). \quad \text{(A3)}$$

Now, the scattering states described by the dipole transition matrices $\boldsymbol{M}_{32\pm1}^{\eta\boldsymbol{k}_f}$ do carry OAM $m = \pm 1$, and hence naturally give rise to circular dichroism in ARPES, as was shown for graphene by multiple scattering calculations [46]. As the relative phase $\zeta(\boldsymbol{k}_f) = \arg(\Sigma_{-1}^{\pm}(\boldsymbol{k}_f)/\Sigma_1^{\pm}(\boldsymbol{k}_f))$ between these scattering waves is clearly a function of the photoelectron's in-plane momentum $\boldsymbol{k}_f$, we further expect this circular dichroism to depend on the kinetic energy, and, correspondingly, on the photon energy used in the experiment, assuming the constant binding energy of the initial state at which the experiment is carried out. Further, as this phase switches sign between the upper (−) and lower (+) Dirac cones, we expect the CD-ARPES asymmetry to invert at the Dirac point, which we show experimentally in Appendix C.

Nondichroic final-state scattering plays a dominant role at kinetic energies where the geometric CD-ARPES produced by the first two terms in the square brackets of Eq. (A2) is suppressed, and provides the main descriptor of the CD-ARPES pattern observed in Fig. 4(a).

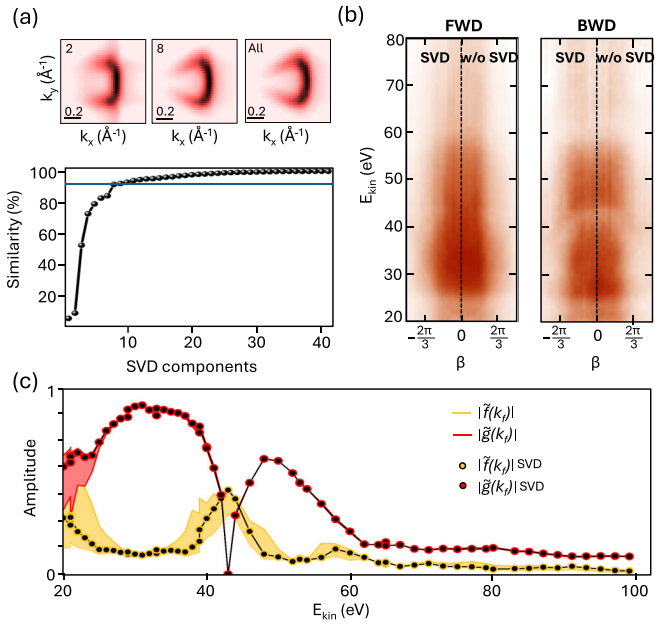

FIG. 7. The impact of noise on the radial cross section of graphene. (a) SVD of the ARPES dataset, which was measured at the MLS at the PTB Berlin, of the graphene horseshoe using 2, 8, and all singular values. The similarity percentage with respect to the full-rank reconstruction is indicated below in the panel. (b) Photoemission intensities around the graphene horseshoe for the OI geometry in the kinetic-energy range from 20 to 80 eV with taking the first eight singular values into account (SVD) and the full-ranked analysis (w/o SVD). (c) Photoemission amplitudes $|\widetilde{g}|$ and $|\widetilde{f}|$ of the s and d channels, respectively, extracted for H-QFMLG as a function of final-state kinetic energy. The curves were extracted from experimental data without and with a singular value decomposition (circles).

APPENDIX B: ROBUSTNESS OF RADIAL CROSS SECTION WITH RESPECT TO NOISE

In the main text, we confirmed that the modulation of intensity within the graphene horseshoe pattern with photon energy remains unchanged when QFMLG is measured on different substrates [Fig. 1(c)]. To verify this, we compared hydrogen-intercalated graphene on 6H-SiC substrates with indenene-intercalated graphene on 4H-SiC substrates. All photon-energy-dependent modulations were consistently reproduced, demonstrating the robustness of the QFMLG sensor.

To test the reliability of the proposed extraction method under nonideal experimental conditions, such as reduced sample quality or the absence of high-resolution measurements, we simulate degraded data quality by restricting the analysis to the leading singular values of the singular value decomposition [47]. This approach emulates the loss of fine-scale information typically encountered in practical experimental settings. Thus, this effectively suppresses higher-order contributions and mimics measurements from samples with lower structural quality. SVD is a mathematical technique that decomposes a dataset into orthogonal components, ranked by their significance, allowing for the identification of dominant trends while filtering out noise and fine-scale information.

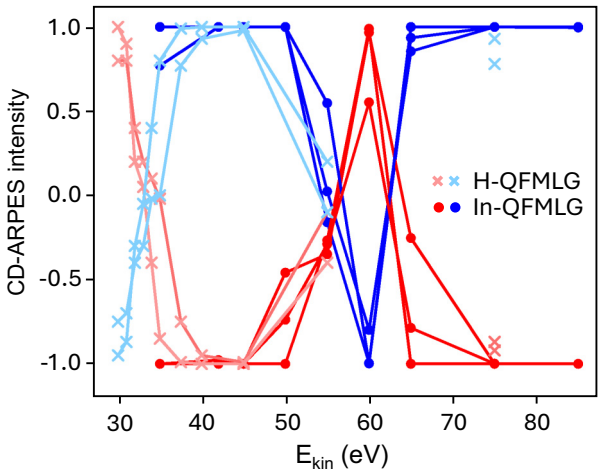

FIG. 8. Measured geometric CD asymmetry in graphene. Circular-dichroism asymmetry of photoemission from In-QFMLG and H-QFMLG, integrated over a circular region of radius $k = 0.2\,\text{Å}^{-1}$ around the K and K′ points [highlighted in Fig. 3(a)], plotted as a function of kinetic energy E_{kin}, separately for each Dirac point. Dark circles correspond to measurements on In-QFMLG with light incidence along the $\text{M}_{\text{Gr}}\Gamma\text{M}_{\text{Gr}}$ direction; light crosses represent data from H-QFMLG with light incidence along the $\text{K}_{\text{Gr}}\Gamma\text{K}'_{\text{Gr}}$ direction [32]. The data in this figure were obtained at Elettra.

By applying SVD to our dataset, we assessed how many components were necessary to accurately describe the measured modulations. Since in the ARPES setup based on a toroidal analyzer, only the photoelectrons emitted in the light-incidence plane finally reach the detector, we rotated the sample around the sample normal in steps of 1° over a 40° range to cover the entire angular range of a graphene horseshoe. This resulted in 41 SVD components, which effectively represent $I(E, k_{||})$ band maps acquired for a particular direction corresponding to the azimuthal orientation of the sample. As a threshold, we defined a 5% deviation as the limit beyond which additional SVD components do not significantly improve the reconstruction of the graphene horseshoe. This restricted the analysis to the eight largest SVD components.

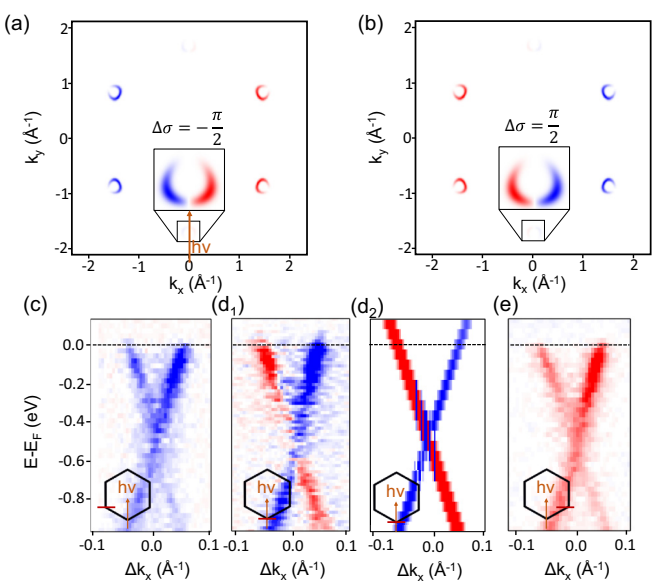

FIG. 9. Geometric CD asymmetry in graphene. Constant-energy maps of photoemission from the graphene valence band calculated using the SWA for the light-incidence plane along the $\text{K}_{\text{Gr}}\Gamma\text{K}'_{\text{Gr}}$ direction with phase shift (a) $\Delta\sigma = -\frac{\pi}{2}$ and (b) $\Delta\sigma = \frac{\pi}{2}$ between the s and d photoemission channels. (c)–(e) CD-ARPES band-structure maps on In-QFMLG along the path shown in the inset, measured at MAESTRO at the ALS with photon energy of 90 eV. **(d_2)** Simulated energy dispersion of graphene along the path shown in the inset using the SWA. The experimental data are explained by phase shift $\Delta\sigma = \pi/2$.

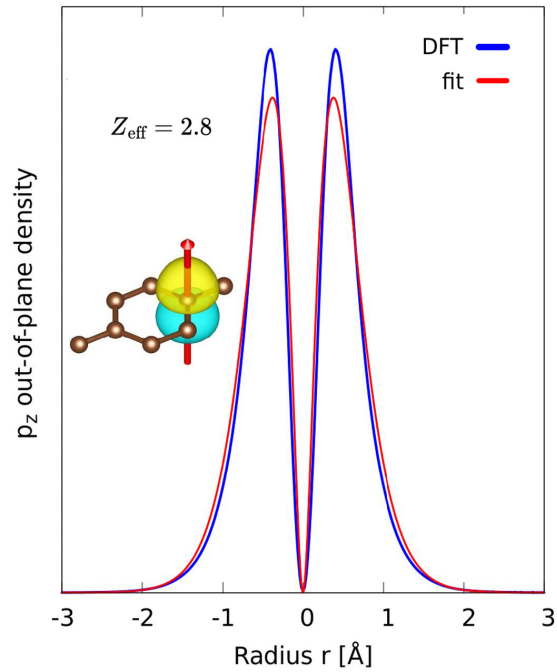

FIG. 10. Effective nuclear charge Z_{eff} seen by photoelectron removed at the Dirac point of graphene, obtained by fitting the DFT-calculated radial charge density of the Bloch state at the K point with a hydrogenic $2p$ radial function, yielding $Z_{\text{eff}} = 2.8$.

The singular values and their threshold are shown in Fig. 7(a), while the photon-energy-dependent modulations, exemplified for the OI geometry for the H-QFMLG sample, are displayed in Fig. 7(b). A comparison with the full-rank analysis (without SVD) shows that the essential features of the extracted quantities remain unchanged. This is further evident from the reconstructed photoemission amplitudes $|\widetilde{g}|$ and $|\widetilde{f}|$ of the s and d channels, which display consistent behavior with (circles) and without (lines) the singular value decomposition in Fig. 7(c), demonstrating the robustness of the reconstruction method.

APPENDIX C: GEOMETRIC CD ASYMMETRY IN GRAPHENE

Figure 3 presents the experimental circular-dichroism asymmetry of In-QFMLG, integrated over a circular region of radius $k = 0.2\,\text{Å}^{-1}$ centered around the K and K′ points, as shown in Fig. 3(a), and plotted as a function of the photoelectron kinetic energy E_{kin} [Fig. 3(b)]. In the main text, for each side of the scattering plane, the three corresponding Dirac points were averaged to enhance visual clarity.

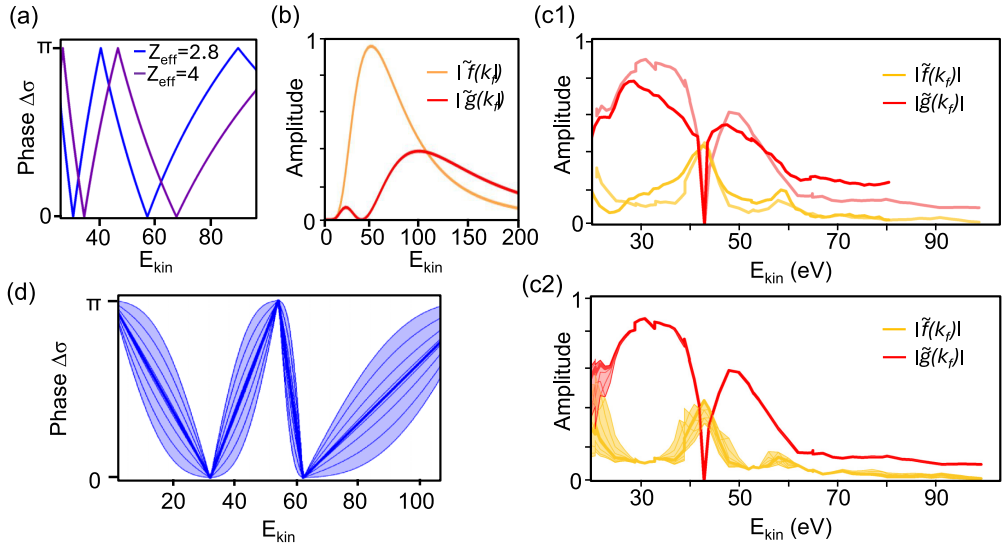

FIG. 11. Comparison of photoemission from hydrogenlike $2p$ orbital and graphene. (a) Calculated Coulomb phase shift $\Delta\sigma$ for atoms with an effective nuclear charge $Z_{\rm eff}$ of 2.8 and 4 (blue and purple curves, respectively). (b) Radial cross sections of photoemission from a hydrogenlike $2p$ orbital with an effective nuclear charge $Z_{\rm eff} = 2.8$. (c) Radial dipole amplitudes $|\widetilde{g}(k_f)|$ and $|\widetilde{f}(k_f)|$ corresponding to the s and d photoemission channels **(c_1)** for In-QFMLG (dark colors) and H-QFMLG (light colors) and **(c_2)** H-QFMLG for the different kinetic-energy-dependent phases in panel (d). (d) Kinetic-energy-dependent phase shifts $\Delta\sigma$, reconstructed experimentally under the assumption of a linear and sinusoidal interpolation between the phase-flip points observed in the CD-ARPES asymmetry.

To assess the contribution of individual valleys, Fig. 8 shows the corresponding analysis performed separately for each Dirac point. Dark circles denote measurements obtained for In-QFMLG with the light incidence aligned along the $M_{\rm Gr}\Gamma M_{\rm Gr}$ direction, whereas light crosses represent data reproduced from H-QFMLG with the light incidence along the $K_{\rm Gr}\Gamma K'_{\rm Gr}$ direction, corresponding to a rotation of the sample by 30°. Despite the different experimental geometries, the overall behavior of the CD asymmetry remains essentially the same. In particular, three pronounced sign reversals of the dichroism are observed at fixed kinetic energies. These features persist across all individual Dirac points, demonstrating the robustness of the observed energy-dependent dichroic response.

So far, we have analyzed the graphene dichroism exclusively in the measurement geometry where the light-incidence plane is oriented along the $M_{\rm Gr}\Gamma M_{\rm Gr}$ direction. In this configuration, no graphene Dirac point lies in the scattering plane. However, when the sample is rotated by 30°, the light-incidence plane aligns with the $K_{\rm Gr}\Gamma K'_{\rm Gr}$ direction, resulting in one K and K′ point each being intersected by the scattering plane. As demonstrated in the main text, the remaining four Dirac points exhibit the same photon-energy behavior as in the previous geometry, namely, a geometric CD asymmetry, which is highlighted in light colors in Figs. 3(b) and 8. It can be accurately described by the SWA simulation shown in Figs. 9(a) and 9(b) for phase shifts $\Delta\sigma = \pm\pi/2$ between the photoemission channels. The corresponding experimental data for three K points at different positions relative to the scattering plane are displayed in Figs. 9(c)–9(e).

When focusing on the graphene K points that lie within the light-incidence plane where the geometric CD asymmetry along the $K_{\rm Gr}\Gamma K'_{\rm Gr}$ direction is naturally suppressed [see Fig. 9(d1)], we observe that the two graphene π bands now exhibit opposite CD asymmetries similar to that shown in Fig. 4. Again, this is to be expected from our nearest-neighbor scattering model described in Appendix A that predicts a sign change of the Daimon effect at the Dirac point.

APPENDIX D: HYDROGENLIKE 2*p* ORBITALS

In photoemission, the Coulomb phase shift

$$\sigma_l = \arg\Gamma(l + 1 + i\eta)$$

arises from the scattering of the outgoing photoelectron by the long-range Coulomb potential of the residual ion. The phase shift between the two dipole-allowed photoelectron emission channels $l \to l \pm 1$ is

$$\Delta\sigma = \sigma_{l+1} - \sigma_{l-1}.$$

The departure of the Coulomb wave from a free-electron plane wave is governed by the Sommerfeld parameter

$$\eta = \frac{Z_{\rm eff}}{a_0 k_f},$$

which quantifies the influence of the ionic potential on the outgoing electron.

To obtain an estimate of the effective ionic charge $Z_{\rm eff}$, we employed VASP to perform density functional theory (DFT) calculations on graphene in the generalized gradient approximation [48,49]. The obtained Bloch states at the Dirac point were projected onto spherical harmonics and squared to obtain the charge density. Cutting the charge density along the out-of-plane direction through a carbon site, we obtain the charge density associated with the graphene Dirac states (blue curve in Fig. 10). Fitting this charge density to the modulus squared

radial wavefunction of a hydrogen $2p$-like orbital

$$\rho(r) \propto (Z_{\text{eff}}/a_0)^5\, r^2\, e^{-Z_{\text{eff}}\, r/a_0}, \tag{D1}$$

we obtain an effective ionic charge of $Z_{\text{eff}} = 2.8$.

Based on this value, we then calculate the Coulomb phase shift $\Delta\sigma$ as a function of the photoelectron kinetic energy and show the result in Fig. 11(a) (blue curves). To assess the impact of variations in Z_{eff} on the phase, we also show calculations for $Z_{\text{eff}} = 4$ (purple curves). We note that Z_{eff} primarily scales the curve along the kinetic-energy axis, while its general shape remains, in particular, the approximate linearity between multiples of π remains unaffected.

The corresponding radial cross sections of these hydrogen-like $2p$ orbitals with an effective nuclear charge Z_{eff} of 2.8, calculated according to Eq. (F17) in Ref. [21], are shown in Fig. 11(b). The s channel displays two maxima separated by a node, while the d channel peaks close to this node. This behavior qualitatively mirrors the reconstructed dipole amplitudes $|\widetilde{g}(k_f)|$ and $|\widetilde{f}(k_f)|$ plotted in Fig. 11(c), supporting our interpretation of the experimental data. The amplitudes extracted for In-QFMLG (dark colors) and H-QFMLG (light colors) in Fig. 11(c1) similarly show good consistency with these trends.

As evident from Fig. 11(a), however, the phase evolution between successive integer multiples of π is only approximately linear within the hydrogenic approximation. To validate this assumption and to test the effect of possible nonlinearity on our amplitude reconstruction, we introduced a sinusoidal modulation of $\Delta\sigma$ between the experimentally determined fixed points [shaded region in Fig. 11(d)]. Reconstructing $|\widetilde{g}(k_f)|$ and $|\widetilde{f}(k_f)|$ for this family of phase variations, we find the resulting radial dipole amplitudes to be remarkably stable, as indicated by the scatter of the curve profile marked in Fig. 11(c2) (for H-QFMLG) by red and yellow shaded areas and several exemplary thin curves, without a significant modification of the shape character and critical points.

APPENDIX E: NORMALIZING THE ARPES INTENSITY OF PRISTINE INDENENE WITH QFMLG

To normalize photoemission intensities for an arbitrary two-dimensional material—here pristine indenene—we proceed in three steps.

First, we perform photon-energy-dependent (and, correspondingly, kinetic-energy-dependent) ARPES measurements of the band of interest. In the present case, ARPES data of pristine indenene were acquired at the I05 beamline of Diamond Light Source using p-polarized light incident at 50° with respect to the surface normal. The ARPES intensity was integrated within a radius of 0.2 Å^{-1} around the indenene Dirac points, which constitute the target system for intensity normalization. The resulting experimental intensity $I_{\text{In}}(k_f)$ is shown as a function of kinetic energy in Fig. 12(b).

Second, keeping the beamline and detector settings unchanged, we perform an analogous measurement on a QFMLG sample to obtain the kinetic-energy-dependent intensity of the graphene Dirac bands, denoted I_{Gr} in Fig. 12(a). For this measurement, the light-incidence plane was aligned along the graphene $\text{K}_{\text{Gr}}\Gamma\text{K}'_{\text{Gr}}$ direction. As before, the ARPES intensity was integrated within a radius of 0.2 Å^{-1} around the graphene Dirac points.

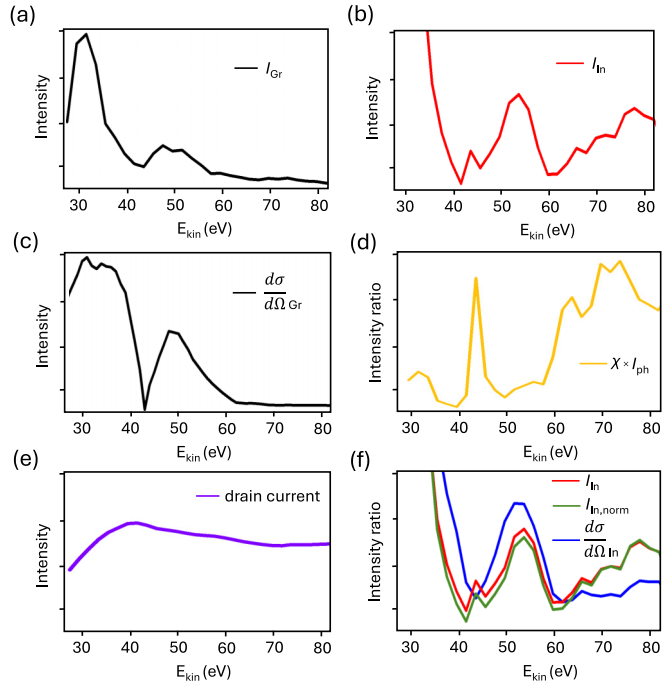

FIG. 12. Normalizing the ARPES intensity of pristine indenene by the QFMLG intensity gauge. ARPES intensity as a function of kinetic energy for (a) graphene and (b) indenene, integrated within a radius of $k = 0.2$ Å^{-1} around respective Dirac points. (c) Calibrated photoemission intensity of graphene (based on $|\widetilde{g}(k_f)|$, $|\widetilde{f}(k_f)|$, and $\Delta\sigma$) for the experimental geometry of the photoemission endstation at the I05 beamline of the Diamond Light Source. (d) Ratio between the experimentally determined intensity and the calibrated photoemission intensity of graphene. This scaling function is proportional to $\chi(k_f)I_{\text{ph}}(h\nu, \boldsymbol{\epsilon})$ of detector and beamline and universally applicable to any sample. (e) Kinetic-energy dependence of the drain current measured on an optical element of the I05 beamline of the Diamond Light Source. (f) Kinetic-energy-dependent photoemission intensity from the indenene valence band (red), after normalization with the drain current (green) and the normalized signal reflecting the differential photoemission cross section of this band (blue).

Third, using the precisely known experimental geometry—namely, the light-incidence direction and polarization with respect to the sample—we calculate the expected differential cross section $\frac{d\sigma}{d\Omega}_{\text{Gr}}$ of the graphene Dirac bands using the SWA model of Eqs. (2) and (3) together with the reconstructed parameters $|\widetilde{g}(k_f)|$, $|\widetilde{f}(k_f)|$, and $\Delta\sigma$. The resulting cross section is shown in Fig. 12(c). According to Eq. (1), the ratio $I_{\text{Gr}}/\frac{d\sigma}{d\Omega}_{\text{Gr}}$ yields the product $\chi(k_f)I_{\text{ph}}(h\nu, \boldsymbol{\epsilon})$ of the kinetic-energy-dependent photon flux and detector response for this experimental configuration [Fig. 12(d)]. Dividing the target intensity I_{In} by this quantity then provides the differential kinetic-energy-dependent cross section $\frac{d\sigma}{d\Omega}_{\text{In}}$ of the indenene valence band up to an overall constant factor, as shown in Fig. 6(c). To benchmark our graphene-based normalization procedure, we compared it with a conventional drain-current-based correction scheme. Figure 12(e) shows the measured drain current of a beamline optical element as a function of photon energy. Such drain-current measurements

are commonly used in ARPES experiments as a proxy for the photon flux, despite generally neglecting the photon-energy dependence of the photoemission quantum efficiency of the monitoring element. The consequences of this approximation are illustrated in Fig. 12(f). The uncorrected ARPES intensity is shown in red, the drain-current-normalized intensity in green, and the differential cross section of indenene, $\frac{d\sigma}{d\Omega}_{\mathrm{In}}$, in blue. While drain-current normalization partially compensates for variations in beamline transmission, substantial discrepancies with the expected cross-section behavior remain. In contrast, normalization using the calibrated graphene reference reveals the differential cross section of indenene, because the graphene response was previously established against an independently calibrated photon-flux dataset, it captures the combined photon-energy dependence of both photon flux and detector response.

[1] S. Moser, An experimentalist's guide to the matrix element in angle resolved photoemission, J. Electron Spectrosc. Relat. Phenom. **214**, 29 (2017).

[2] D. Lüftner *et al.*, Imaging the wave functions of adsorbed molecules, Proc. Natl. Acad. Sci. USA **111**, 605 (2014).

[3] P. Puschnig and M. Ramsey, Photoemission tomography: Valence band photoemission as a quantitative method for investigating molecular films, edited by K. Wandelt *Encyclopedia of Interfacial Chemistry* (Elsevier, Oxford, 2018), p. 380.

[4] J. Erhardt *et al.*, Bias-free access to orbital angular momentum in two-dimensional quantum materials, Phys. Rev. Lett. **132**, 196401 (2024).

[5] M. Schüler *et al.*, Local Berry curvature signatures in dichroic angle-resolved photoelectron spectroscopy from two-dimensional materials, Sci. Adv. **6**, eaay2730 (2020).

[6] M. Kang *et al.*, Measurements of the quantum geometric tensor in solids, Nat. Phys. **21**, 110 (2025).

[7] S. Weiß *et al.*, Exploring three-dimensional orbital imaging with energy-dependent photoemission tomography, Nat. Commun. **6**, 8287 (2015).

[8] P. J. Feibelman and D. E. Eastman, Photoemission spectroscopy—Correspondence between quantum theory and experimental phenomenology, Phys. Rev. B **10**, 4932 (1974).

[9] J. W. Gadzuk, Surface molecules and chemisorption. II. Photoemission angular distributions, Phys. Rev. B **10**, 5030 (1974).

[10] G. D. Mahan, Theory of photoemission in simple metals, Phys. Rev. B **2**, 4334 (1970).

[11] N. V. Smith, M. M. Traum, J. A. Knapp, J. Anderson, and G. J. Lapeyre, Polarization effects in angle-resolved photoemission using synchrotron radiation, Phys. Rev. B **13**, 4462 (1976).

[12] G. Lapeyre, J. Anderson, and R. Smith, Initial state symmetries from polarization effects in angular resolved photoemission, Surf. Sci. **89**, 304 (1979).

[13] A. Bansil and M. Lindroos, Importance of matrix elements in the ARPES spectra of BISCO, Phys. Rev. Lett. **83**, 5154 (1999).

[14] A. Bansil and M. Lindroos, Matrix element effects in the angle-resolved photoemission spectrum of BISCO, J. Phys. Chem. Solids **59**, 1879 (1998).

[15] P. Puschnig *et al.*, Orbital tomography: Deconvoluting photoemission spectra of organic molecules, Phys. Rev. B **84**, 235427 (2011).

[16] W. S. Jung *et al.*, Imaging the electron density in solids by using multi-Brillouin-zone angle resolved photoelectron spectroscopy, Phys. Rev. B **82**, 235105 (2010).

[17] D. Lee and C. Kim, Method to map one-dimensional electronic wave function by using multiple Brillouin zone angle resolved photoemission, JAST **1**, 118 (2010).

[18] S. Moser, A toy model for dichroism in angle resolved photoemission, J. Electron Spectrosc. Relat. Phenom. **262**, 147278 (2023).

[19] E. E. Krasovskii, Character of the outgoing wave in soft x-ray photoemission, Phys. Rev. B **102**, 245139 (2020).

[20] V. N. Strocov *et al.*, High-energy photoemission final states beyond the free-electron approximation, Nat. Commun. **14**, 4827 (2023).

[21] C. S. Kern *et al.*, Simple extension of the plane-wave final state in photoemission: Bringing understanding to the photon-energy dependence of two-dimensional materials, Phys. Rev. Res. **5**, 033075 (2023).

[22] J. Erhardt *et al.*, Indium epitaxy on SiC(0001): A roadmap to large scale growth of the quantum spin Hall insulator indenene, J. Phys. Chem. C **126**, 16289 (2022).

[23] A. K. Geim, Graphene: Status and prospects, Science **324**, 1530 (2009).

[24] C. Riedl, C. Coletti, and U. Starke, Structural and electronic properties of epitaxial graphene on SiC(0001): A review of growth, characterization, transfer doping and hydrogen intercalation, J. Phys. D: Appl. Phys. **43**, 374009 (2010).

[25] A. Gottwald *et al.*, Current capabilities at the Metrology Light Source, Metrologia **49**, S146 (2012).

[26] C. Schmitt *et al.*, Achieving environmental stability in an atomically thin quantum spin Hall insulator via graphene intercalation, Nat. Commun. **15**, 1486 (2024).

[27] S. Glass *et al.*, Atomic-scale mapping of layer-by-layer hydrogen etching and passivation of SiC(0001) substrates, J. Phys. Chem. C **120**, 10361 (2016).

[28] T. Seyller, Passivation of hexagonal SiC surfaces by hydrogen termination, J. Phys.: Condens. Matter **16**, S1755 (2004).

[29] N. Briggs *et al.*, Atomically thin half-van der Waals metals enabled by confinement heteroepitaxy, Nat. Mater. **19**, 637 (2020).

[30] H. Kim, N. Tsogtbaatar, B. Tuvdendorj, A. Lkhagvasuren, and J. M. Seo, Effects of two kinds of intercalated In films on quasi-free-standing monolayer graphene formed above SiC(0001), Carbon **159**, 229 (2020).

[31] L. Broekman *et al.*, First results from a second generation toroidal electron spectrometer, J. Electron Spectrosc. Relat. Phenom. **144–147**, 1001 (2005).

[32] H. Boban *et al.*, Scattering makes a difference in circular dichroic angle-resolved photoemission, Phys. Rev. B **111**, 115127 (2025).

[33] M. Bauernfeind *et al.*, Design and realization of topological Dirac fermions on a triangular lattice, Nat. Commun. **12**, 5396 (2021).

[34] J. Sforzini *et al.*, Approaching truly freestanding graphene: The structure of hydrogen-intercalated

graphene on 6H-SiC(0001), Phys. Rev. Lett. **114**, 106804 (2015).

[35] C. S. Kern *et al.*, Circular dichroism in the photoelectron angular distribution of achiral molecules, Phys. Rev. Res. **8**, 023275 (2026).

[36] I. Gierz, M. Lindroos, H. Höchst, C. R. Ast, and K. Kern, Graphene sublattice symmetry and isospin determined by circular dichroism in angle-resolved photoemission spectroscopy, Nano Lett. **12**, 3900 (2012).

[37] Y. Liu, G. Bian, T. Miller, and T.-C. Chiang, Visualizing electronic chirality and Berry phases in graphene systems using photoemission with circularly polarized light, Phys. Rev. Lett. **107**, 166803 (2011).

[38] C. Hwang *et al.*, Direct measurement of quantum phases in graphene via photoemission spectroscopy, Phys. Rev. B **84**, 125422 (2011).

[39] H. Daimon *et al.*, Strong circular dichroism in photoelectron diffraction from nonchiral, nonmagnetic material–direct observation of rotational motion of electrons, Jpn. J. Appl. Phys. **32**, L1480 (1993).

[40] C. Schmitt, R. Claessen, and S. Moser, Dataset: Turning graphene into an intensity gauge for ARPES, University of Würzburg, WueData, 2026, doi: 10.58160/uaabat31rcvf42nu.

[41] J. W. Cooper, Photoionization from outer atomic subshells. A model study, Phys. Rev. **128**, 681 (1962).

[42] S. Moser *et al.*, Polarization control at the microscopic and electronic structure observatory, Nucl. Instrum. Methods Phys. Res. Sect. A **914**, 156 (2019).

[43] M. Mulazzi *et al.*, Understanding intensities of angle-resolved photoemission with circularly polarized radiation from a Cu(111) surface state, Phys. Rev. B **79**, 165421 (2009).

[44] J. Avery, Many-center Coulomb Sturmians and Shibuya-Wulfman integrals, Int. J. Quantum Chem. **100**, 121 (2004).

[45] V. Aquilanti and A. Caligiana, Sturmian approach to one-electron many-center systems: Integrals and iteration schemes, Chem. Phys. Lett. **366**, 157 (2002).

[46] P. Krüger and F. Matsui, Observation and theory of strong circular dichroism in angle-revolved photoemission from graphite, J. Electron Spectrosc. Relat. Phenom. **258**, 147219 (2022).

[47] G. H. Golub and C. Reinsch, Singular value decomposition and least squares solutions, Numer. Math. **14**, 403 (1970).

[48] G. Kresse and J. Furthmüller, Efficient iterative schemes for *ab initio* total-energy calculations using a plane-wave basis set, Phys. Rev. B **54**, 11169 (1996).

[49] J. P. Perdew, K. Burke, and M. Ernzerhof, Generalized gradient approximation made simple, Phys. Rev. Lett. **77**, 3865 (1996).